2025-06-01
lamport*-robust

Laser-Induced Diaphragm Rupture for Improved Sequencing and Repeatability in a Hypersonic Facility

Byrenn Birch[1], David Buttsworth[2] and Fabian Zander[3]
University of Southern Queensland, Toowoomba, 4350, Australia

For hypersonic facilities where the flow conditions are established through the rupture of a diaphragm, such as in the University of Southern Queensland's TUSQ facility, the variability in the flow conditions is related to the uncertainty of the pressure at which the diaphragm ruptures. Variability in the diaphragm rupture pressure also results in uncertainty of the time at which the diaphragm will rupture. For experiments which require knowledge of when the test flow will be initiated, the sequencing of events relative to the flow onset is difficult when the flow is initiated using the natural rupture of a diaphragm. The challenge of experiment sequencing that arises due to rupture pressure variability is addressed by introducing a laser for rapid thermal weakening of the diaphragm. Event sequencing challenges are discussed in the context of free-flight testing, including model release strategies for such testing. The work proceeds through a review of Ludwieg tube flow initiation strategies, and a discussion of the present context which requires a reliable method for sequencing the retraction of the free flight model holder. The natural variability of strength of the Mylar diaphragms in the present work is found to result in around ±6 % uncertainty in rupture pressure. This rupture pressure variability is demonstrated to have a significant temperature dependence, through empirical results and engineering models. Implementation of the laser-induced diaphragm rupture method is demonstrated to enhance repeatability in generating the flow conditions; the variability in rupture pressure was reduced to ±2 % when the laser method was used. Based on the remaining sequencing uncertainties with the laser-induced rupture method and practical speeds for model platform retraction, uncertainty in the positioning of the free flight models at the time of flow onset is shown to be ±2 mm.

I. Nomenclature

A = Area

[1]Lecturer, School of Mechanical and Electrical Engineering, AIAA Member.
[2]Professor, School of Mechanical and Electrical Engineering, AIAA Member.
[3]Senior Research Fellow, Institute of Advanced Engineering and Space Sciences, AIAA Member.

c = Specific heat

D = Diameter

k = Thermal conductivity

P = Pressure

R, r = Radius

T = Temperature

t = Time

x = Axial distance

y = Vertical distance

α = Thermal diffusivity

Δ = Undeformed material thickness

δ = Material thickness

ϵ = Strain

θ = Angle

ρ = Density

σ = Stress

II. Introduction

New Ludwieg tube facilities have recently been commissioned at academic institutions [1, 2] and other laboratories [3] around the globe and their popularity stems from low capital and operating costs, as well as their versatility across a range of hypersonic aerodynamic ground test applications. Ludwieg tubes are expected to play a significant role in world-wide hypersonic research efforts on access-to-space and hypersonic cruise technologies.

Hypersonic flow in Ludwieg tubes is typically initiated by either the actuation of a fast-acting plug valve or the rupture of one or more diaphragms. If a plug valve is used, the period for establishment of a steady flow at the nozzle exit is likely to be dictated by the valve opening time. The Hypersonic Ludwieg Tube Braunschweig (HLB) valve opening time is ~ 10 ms for an axial movement of about 50 mm [4] and the Air Force Research Laboratory Ludwieg tube has a valve opening time of ~ 20 ms [3]. Although faster steady flow establishment can be achieved if diaphragms are used, valves have the advantage that they can be closed after a period of time, potentially preserving a significant fraction of the high pressure test gas for subsequent experiments.

Different designs for Ludwieg tube plug valves have been successfully demonstrated. The Hypersonic Ludwieg Tube Braunschweig (HLB) operates using a valve with a downstream-facing seat [4] whereas the Oxford High Density Tunnel (HDT) operates with an upstream-facing valve seat [5]. The transient filling and discharge of the plenum chamber

which is positioned between the valve and the nozzle throat in the HDT facility induces an unsteady flow start-up period of about 40 ms [6]. In the case of the HLB facility, vorticity in the valve wake convects through the nozzle and has a measurable effect on the flow quality: a cone probe with a PCB pressure sensor registered nRMS-values about 30 % higher on centre line relative to values at between 100 mm to 150 mm radius [7]. When using a plug valve arrangement in the Air Force Research Laboratory (AFRL) facility, nozzle exit RMS Pitot pressure fluctuations were about 50 % higher than registered when using a fully-opened, single diaphragm positioned upstream of the nozzle throat [3].

Positioning the diaphragm station downstream of the test section is preferred when seeking quiet Ludwieg tube operation because diaphragms positioned upstream of the nozzle throat can induce disturbances that corrupt the nozzle flow and diaphragm debris can potentially scratch highly polished nozzle surfaces [8]. When using Ludwieg tubes with downstream diaphragms, the test section needs to be rated to the full operating pressure of the Ludwieg tube which poses significant mechanical design constraints on the facility. Although diaphragm opening can occur in less than one millisecond, the establishment of hypersonic nozzle flow with downstream diaphragm/s, which depends on isentropic wave propagation upstream and past the nozzle throat, will still take around ten milliseconds or longer for typical nozzle and test section lengths. If quiet tunnel operation is not required, but rapid steady flow onset is valuable to the planned experiments, then an upstream diaphragm arrangement can be used. However, if the planned experiments also require repeatable sequencing of the diaphragm rupture, some additional system or device is typically required because of the natural variability in diaphragm strength which can be around ±6 % or higher.

One common approach for controlled diaphragm rupture is to use a double diaphragm arrangement [8] which typically involves: (1) two diaphragms, each designed to rupture at a pressure differential somewhat higher than 50 % of the target Ludwieg tube operating pressure; (2) a cavity between the diaphragms which is maintained at a pressure approximately half of the target operating pressure when preparing for an experiment; and (3) flow initiation by either increasing or decreasing the cavity pressure until one of the diaphragms ruptures, with the other diaphragm following quickly thereafter. In this arrangement it is possible to accurately sequence the initiation of the flow onset using only diaphragms and a pressure regulation system. However, the full-opening of a single diaphragm is easier to implement and is more readily achieved than in double diaphragm arrangements that typically require substantial development effort [3].

Controlling the rupture of single diaphragm can also be achieved through various systems. A diaphragm-piercing fixture on a ram can be actuated to control diaphragm rupture [9]. However, such a piercing system is likely to present some degree of flow blockage, potentially generating measurable wake effects similar to fast-acting valve systems. The electromagnetic actuation of a copper wire designed to tear a Mylar diaphragm was investigated in the context of expansion tube performance [10]. The results were somewhat inconclusive, but it was noted that electromagnetic interference on other sensors was significant [10]. Single Mylar diaphragms have also been ruptured successfully using thermal effects induced by: (1) Nichrome heating wires in contact with the diaphragm [8]; and (2) laser energy

deposition [11]. Testing of the laser-induced diaphragm rupture for a shock tube [11] was limited to pressure differentials of 9.4 kPa with the gas either side of the diaphragms at the same temperature. The laser source was positioned outside of the shock tube facility where the high-pressure side was at atmospheric pressure. For hypersonic test facilities, direct line-of-sight to the diaphragm from outside the test facility is not generally possible. In theory, this line-of-sight limitation can be overcome by: (1) turning the beam via an array of mirrors; (2) using a fibre-coupled laser; or (3) mounting the laser inside the test facility. The power of the laser must be sufficiently high to rapidly and reliably burst the diaphragm, however excessive laser power is known to induce pressure fluctuations in the post-shock flow of a shock tube [11].

The Ludwieg tube considered herein uses a nominally isentropic compression of the test gas via the action of a free piston, and fast initiation of flow onset is desired for free flight model testing purposes. Therefore, the preferred arrangement is a single diaphragm positioned upstream of the nozzle throat. As the free piston comes to rest at the inlet of the hypersonic nozzle and thereby terminates the hypersonic flow, it is also preferable to avoid mechanical actuation systems in the tube upstream of the diaphragm. The present work represents an extension of the laser rupture approach introduced by [11] in several important respects. (1) Line-of-sight to the diaphragm from outside the test facility was not possible, so we have demonstrated a system with the laser mounted inside the test section with a direct view of the diaphragm upstream through the hypersonic nozzle. (2) A model for thermal weakening of the diaphragm due to transient heating from piston compression and the laser energy input provides theoretical tools for future diaphragm and rupture system design. (3) A reliable diaphragm rupture system for highly repeatable sequencing of free flight experiments is demonstrated and has the additional benefit of improving the repeatability of flow condition generation.

III. TUSQ Facility and Free-Flight Experimental Methods

A. Facility Overview

The University of Southern Queensland's Ludwieg tube with free piston compression heating (TUSQ, Fig. 1) is used to generate quasi-steady cold hypersonic flows for test durations of the order of hundreds of milliseconds. Prior to firing, the facility comprises three discrete volumes of gas: (1) the 350 L high pressure air reservoir; (2) the air in the Ludwieg tube (or barrel); and (3) the low pressure (< 1 kPa) region within the nozzle, test section and dump tanks. For the condition analysed herein (Table 1), the test gas initially in the barrel is at the local atmospheric pressure and ambient temperature (approximately 94 kPa and 24 °C in Toowoomba). A piston is positioned in the barrel immediately downstream of the primary valve and a Mylar diaphragm separates the barrel and nozzle inlet. To date, a 346 g nylatron piston has been commonly used. For the work reported herein, a 100 µm thick Mylar diaphragm was used.

A run is initiated by opening the pneumatically-actuated primary valve which causes the piston to be driven along the barrel by the flow of high pressure air from the reservoir, compressing the test gas. The pressure in the barrel is

measured by a PCB113A03 piezoelectric pressure transducer positioned 225 mm upstream of the nozzle entrance. By relatively slow primary valve opening over a period of about 0.5 s, the occurrence of discrete compression waves can be virtually eliminated during the nominally isentropic compression process. Compression continues until the diaphragm ruptures, which then allows gas to leave the barrel and accelerate through the nozzle as the test flow.

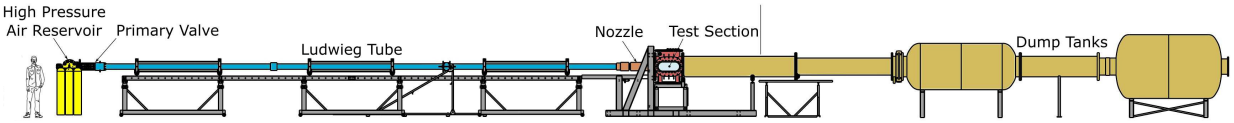

Fig. 1 Schematic of the TUSQ facility.

Table 1 Nominal test conditions for the work herein.

Stagnation pressure	1 MPa
Stagnation temperature	575 K
Static pressure	670 Pa
Static temperature	71 K
Mach number	5.95
Unit Reynolds number	7.17×10^6 m^{-1}

B. Model Release Strategies for Free-Flight Experiments

1. Prior work

Free flight experiments in the TUSQ facility initially used a system in which models were slung beneath a retractable rod and were firmly held in place against a molded head on the rod prior to tunnel firing using a highly tensioned string [12]. Prior to diaphragm rupture, the string was cut with a razor blade, and the model fell away from the molded head under the action of gravity. Following model release and initial separation from the molded head, the rod was retracted out of the flow. The model suspension and string tensioning arrangement was normally configured so that the severed string did not impart roll to the model during the release process, however this could not always be ensured. The thread cutter arrangement also had limited versatility as models were only supported at one location and were susceptible to sliding along the string as well as pitching or rolling during routine facility operations prior to the run, such as test section evacuation.

The sequencing of this system relied upon the barrel pressure signal and natural diaphragm rupture. In addition to the variability of diaphragm burst pressure, there is variation of the nominally 1.4 MPa s^{-1} linear pressure rise in the

barrel prior to diaphragm rupture, in the case of the Mach 6 nozzle operating condition. When triggers and timing systems are based on a rising-edge voltage signal from the barrel pressure transducer, the onset of flow relative to this voltage threshold is a function of both the rate of pressure rise in the barrel and the variability of the diaphragm rupture pressure.

2. *Current approach*

To achieve a reliable model release that does not impart moments on the model, a platform that retracted rapidly from below the model was desired. However, due to facility size and functionality constraints, a simple linear translating platform was not feasible. Instead, an improved arrangement involving a rapidly-retracted platform attached to a Chebyshev lambda mechanism (see Fig. 2) was implemented and this device has since been used successfully in several free flight campaigns [13, 14].

The mechanism initially moves vertically downwards and imparts no measurable rotation to the model during separation, as the theoretical results in Fig. 3 illustrate. From the results in Fig. 3a, for the first 1 mm of travel, the platform moves in the streamwise direction by less than 0.002 mm and the platform rotates by less than 0.003°. From the results in Fig. 3b and Fig. 3c, for the first 0.15 mm of initial vertical movement, the velocities and accelerations in the vertical direction exceed those in the horizontal direction by at least three orders of magnitude.

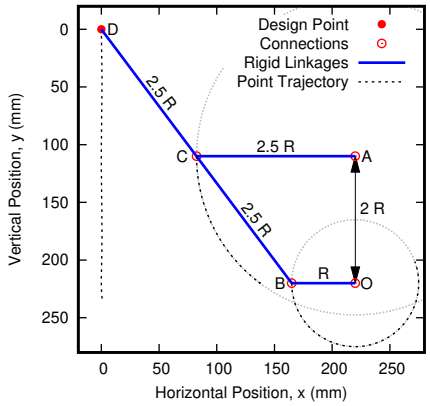

(a) Model platform design curve.

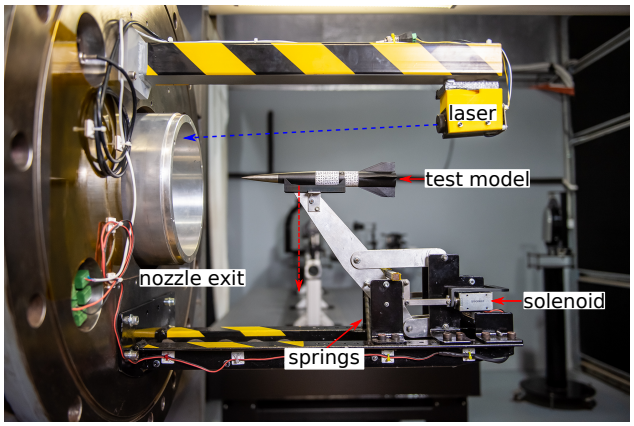

(b) Image of the Chebyshev model release mechanism.

Fig. 2 Chebyshev lambda mechanism illustrating: (a) the physical size of the mechanism; and (b) the device in the test section of TUSQ.

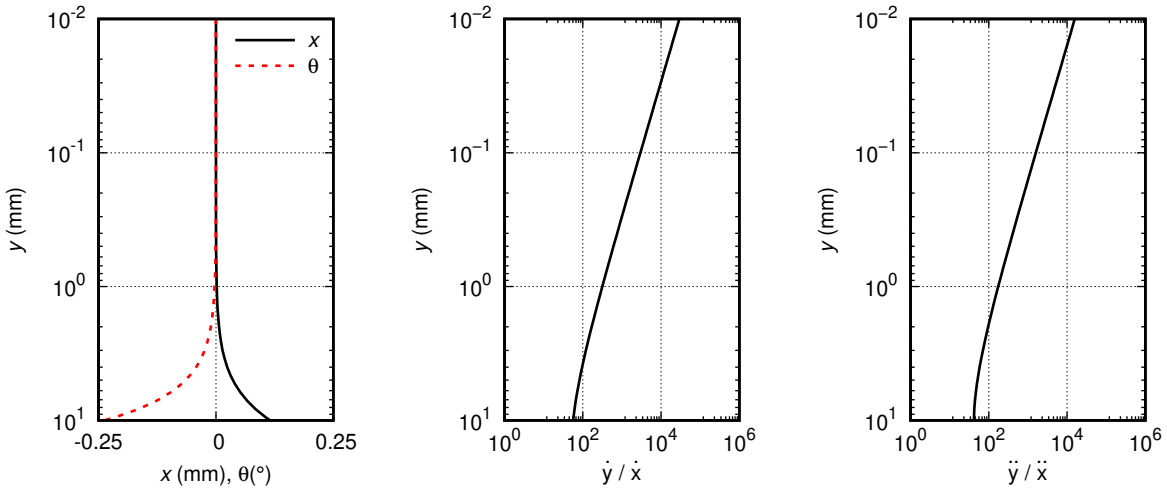

(a) Platform trajectory and angle. **(b) Platform velocity ratios.** **(c) Platform acceleration ratios.**

Fig. 3 Design performance of the Chebyshev mechanism showing that the platform falls vertically at zero angle of attack for the first few millimetres of travel.

The linkages in the physical realization of the mechanism are fabricated from aluminium sheet 2 mm thick, and with the mechanism in its initial position (linkages AC and OB in the horizontal position), springs provide a pre-load of about 34 N in the vertical direction, with a spring constant of about 490 N m^{-1} for this extension. The mechanism is held in its initial position against the downward force from the springs using two solenoids (one on either side of the device) which are energised to initiate the actuation at the appropriate time. Over the first 5 mm of vertical motion, the average vertical acceleration of the platform is approximately 112 m s^{-2}. The platform travels downwards by approximately 100 mm taking the platform out of the core flow zone of the nozzle exit within 70 ms of solenoid actuation. This mechanism overcomes the challenges of a thread-cutter arrangement and offers a reliable method for controlled model insertion into the flow. However, variability in the timing of diaphragm rupture relative to the voltage threshold from the barrel pressure transducer was still causing a large number of free flight runs to be lost because of poor release sequencing relative to flow onset.

C. Motivation: Improving Facility Pressure Repeatability and Experiment Event Timing

The volumetric flow rate through the primary valve is normally designed to match the discharge through the hypersonic nozzle throat after diaphragm rupture, and under these conditions, the pressure of the test gas in the nozzle supply region is quasi-steady. For given initial conditions in the barrel, the rupture pressure of the diaphragm therefore controls the nozzle supply flow conditions. Consequently any variability in the diaphragm rupture pressure is manifest as variability in the hypersonic flow conditions. This is the *first motivation* for the laser-induced diaphragm rupture method for TUSQ: it is preferable to have a facility operating strategy such that high *repeatability of flow conditions* can be achieved.

The variability in rupture pressure of Mylar diaphragms may be partially explained by several factors, including variations in film thickness, but temperature effects certainly play a role. Fig. 4 presents the measured Mylar diaphragm burst pressure when using the Mach 6 nozzle with an initial air pressure in the barrel prior to piston compression of approximately 94 kPa (absolute), with the initial temperature of this air being equal to the ambient laboratory temperature. The 'natural rupture' results in Fig. 4 appear to correlate with the ambient temperature ($R^2 = 0.48$) with the slope of this correlation being $-4.48\,\text{kPa}\,^\circ\text{C}^{-1}$. This slope aligns reasonably well with the theoretical 'temperature sensitivity' result of $-5.07\,\text{kPa}\,^\circ\text{C}^{-1}$, the derivation of which is explained in Section V.

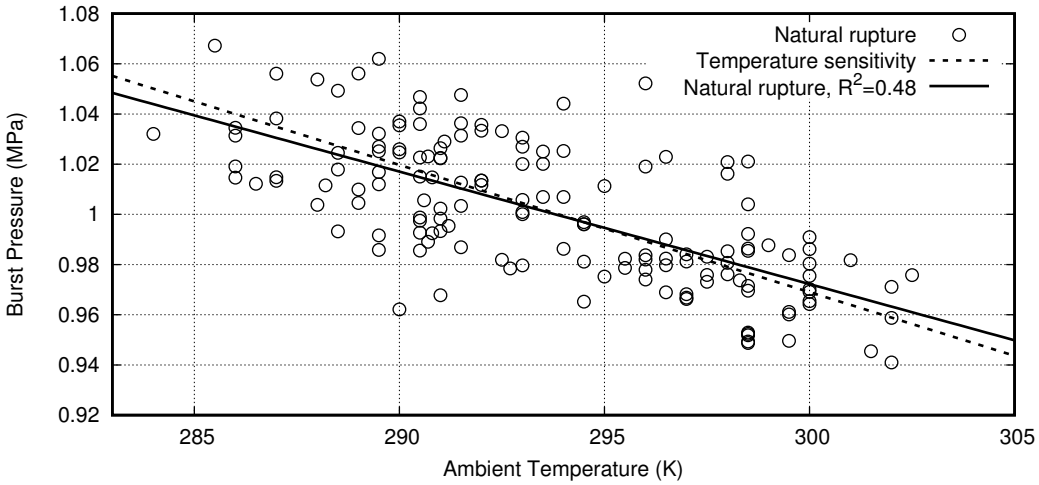

Fig. 4 Diaphragm burst pressure for the Mach 6 nozzle as a function of ambient temperature.

The total flow duration within TUSQ is on the order of 200 ms, and the flow onset at the nozzle exit occurs within milliseconds of diaphragm rupture. To take advantage of the step-like aerodynamic loading with flow onset and maximise the productivity of each run, initiation of the model release for free-flight experiments needs to occur prior to diaphragm rupture. The event trigger for such actuation in TUSQ experiments is the rising edge voltage threshold for the barrel pressure transducer signal. Variations of the diaphragm rupture pressure, and the variation of the rate of pressure rise during piston compression, significantly impact the timing of model release actuation. Improving the *repeatability of event sequencing* is the *second motivation* for the laser-induced diaphragm rupture method for TUSQ.

IV. Diaphragm Rupture Experiments

A. Laser Method for Flow Repeatability and Event Sequencing

To improve the run-to-run pressure repeatability in TUSQ and the success rate of free-flight testing, a laser-induced diaphragm rupture system was developed where the energy from the laser is used to rapidly thermally weaken the diaphragm. With this system, a low cost 5 W, 450 nm collimated laser module (OdicForce OFL365-5-TTL3) is positioned within the test section as illustrated in Fig. 2b. Direct line-of-sight from the laser output to the centre of the

100 µm Mylar diaphragm was provided using a 3d printed a custom laser module mount, which was placed so that it: (1) does not interfere with the core hypersonic flow produced by the facility; and (2) does not limit optical access for flow diagnostics, such as the schlieren imaging system. The Mylar diaphragm stock used in this work was transparent; to increase the absorption of the laser energy, the diaphragm was coated in a thin layer of flat black acrylic paint on the side facing the laser at the location where the energy from the laser pulse is deposited. Measurements on representative samples of the painted diaphragms using a micrometer indicate a paint layer thickness of 27±10 µm.

To determine the energy deposited by the laser, a 20 µm diameter pinhole was mounted to a photodetector (Thorlabs PDA36A2) and this assembly was traversed across and along the laser beam. To measure the size of the laser beam, the distance between the photodetector and laser head was 1.3 m, similar to the distance between the laser head and a diaphragm for a typical run of the TUSQ facility. The responsivity of the photodetector at 450 nm was 0.114 A W^{-1} and the photodetector-oscilloscope pair was set to 2.38×10^6 V A^{-1}. Measurements were made at intervals $\Delta x = 0.2$ mm and $\Delta y = 0.1$ mm for the coordinate system shown in Figure 5. The beam profile at the diaphragm station was found to be approximately 7.9 mm × 0.29 mm FWHM with a Gaussian distribution of power across the short axis. Integrating the beam profile shown in over the identified beam size results in a measured beam power of 4.05 W which is favourable relative to the nominal 5 W optical power of the laser module.

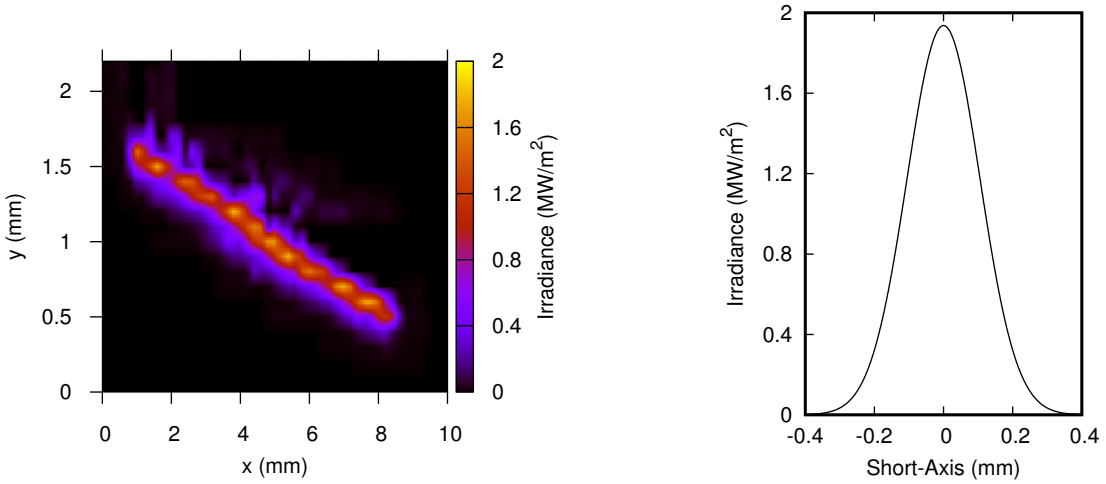

(a) Distribution of laser energy.

(b) Typical cross-section of laser profile.

Fig. 5 Measured profile of the laser where the sample region was limited by a 20 µm diameter pinhole.

B. Timing and Sequencing System

A timing system is used to properly sequence the diaphragm rupture at the desired pressure, and has the capability to sequence other timing-critical events such as the release of a free-flight test model. The flow timing and event sequencing system operation is demonstrated in Figure 6. This system currently utilises a PICAXE 40X2 as the facility sequencing driver, receiving the barrel pressure as the input and driving the required output triggers. The voltage output

of the barrel pressure transducer is measured and, when the voltage reaches a predefined level, the PICAXE is used to determine the rate of voltage increase over a defined period of time, as the rate of voltage increase cannot be assumed as constant across separate runs of the TUSQ facility. This rate of voltage increase is used to predict the remaining time until the pressure in the barrel reaches the defined burst pressure, thereby predicting the barrel pressure until diaphragm rupture. The laser is activated to initiate the rupture process, with the laser on TTL pulse beginning a few milliseconds prior to the desired rupture to allow sufficient time for the diaphragm to be weakened by the laser. For the case of free flight experiments, the test model must be released prior to flow initiation and with sufficient time for the model release mechanism to clear the flow region. The TUSQ Chebyshev mechanism requires approximately 70 ms after the model release signal is initiated to retract clear of the flow, therefore the signal to release the model must precede the desired diaphragm rupture event by at least 70 ms.

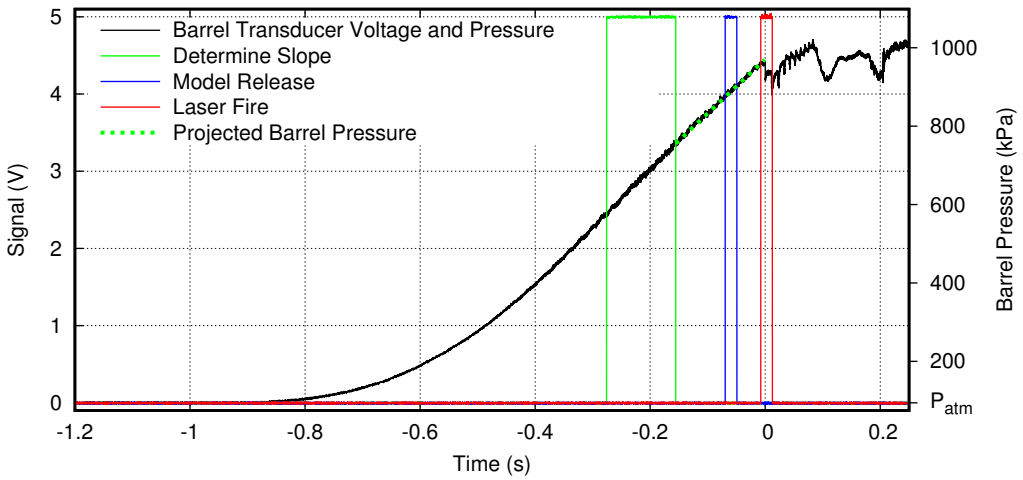

Fig. 6 Demonstration of the flow timing and event sequencing system performance from Run 1033. The time axis has been set so that the diaphragm rupture occurs at $t = 0$.

C. Pressure Repeatability

The diaphragm burst pressure (P_B), assuming the facility is tuned to the matched condition, is the quasi-steady nozzle supply pressure for the duration of the run. Pressure oscillations caused by finite piston mass effects and the propagation of pressure waves in the barrel result in oscillations about the diaphragm burst pressure of $\overline{P_{B\,-10\%}^{+6\%}}$ when the 346 g nylatron piston is used. These barrel pressure oscillations, when combined with noise which radiates from the boundary layer on the nozzle wall, results in Pitot pressure fluctuations of 2.52 % (0.3 kHz to 25 kHz) [15] and RMS density fluctuations of 0.4 % (1 kHz to 250 kHz) [16] within the Mach 6 freestream. Additionally, the ±5.6 % run-to-run variability of the diaphragm burst pressure results in uncertainty in the freestream conditions which will be produced for a particular run. By reducing the variability of the diaphragm rupture condition, the uncertainty of the flow conditions is therefore reduced.

The barrel pressure data from 156 runs at the most commonly used Mach 6 condition (see Table 1) with natural diaphragm rupture, and from 16 runs at this same nominal condition using the laser-induced diaphragm rupture were analysed to determine the variability of the diaphragm burst pressure. For natural diaphragm rupture, the diaphragm burst pressure was 998 kPa ± 5.6 % as shown in Figure 7, where ±5.6 % represents two standard deviations (2σ) from the mean. To implement a forced diaphragm rupture of the same diaphragm stock, the average burst pressure must be reduced to avoid prohibitively early natural diaphragm rupture. The target burst pressure was set to 970 kPa (a 2.7 % reduction from natural rupture) which, as shown in Figure 7a, preserved the burst pressure within the band of the natural diaphragm rupture condition. The 2σ value reduced from 5.6 % for natural diaphragm rupture to 2.2 % for laser-induced diaphragm rupture. Since the value of diaphragm burst pressure was maintained within the uncertainty bounds of natural rupture, previous flow characterisation efforts, both time-averaged and the fluctuating components, for this condition are expected to remain valid.

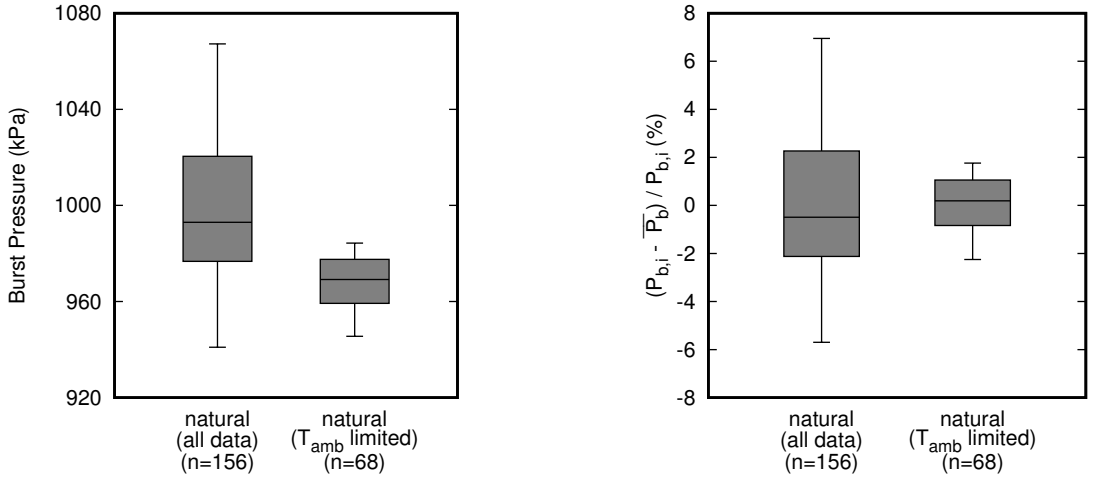

(a) Diaphragm rupture pressure. **(b) Percentage variation from mean rupture pressure.**

Fig. 7 Diaphragm rupture pressure statistics for the natural conditions.

D. Timing and Sequencing Repeatability

In addition to the improved facility pressure repeatability that can be achieved through use of a laser-induced diaphragm rupture, significant improvements were made to the success rate of timing-critical experiments such as free-flight. These experiments require that the model is suspended in the test section and released just prior to flow initiation, but with sufficient time for the release mechanism to clear the flow.

Previously, the timing of the model release was controlled by a simple rising edge threshold of the barrel pressure transducer signal. To compare the uncertainly of the flow initiation timing for the previously used method with natural diaphragm rupture and the new laser-induced diaphragm rupture system, the delay to diaphragm rupture from a known event has been used. For the natural diaphragm rupture, the reference event was when the output from the barrel

pressure passed through the equivalent of 4 V at the presently used charge amplifier settings (400 kPa V^{-1}) in Figure 6. This voltage level precedes natural diaphragm rupture by a timescale similar to the retraction time of the Chebyshev model release mechanism. For the laser-induced diaphragm rupture, the time between diaphragm rupture and the model release was used.

The variability of timing for the flow initiation is shown in Figure 8 on and absolute scale in (a) and a scale relative to the mean delay in (b). A significant timing uncertainty reduction from $2\sigma = \pm 27.9$ ms to $2\sigma = \pm 2.5$ ms was achieved. The practical implications of improved facility sequencing are well demonstrated by free-flight experiments, however the facility sequencing improvements are significant for any experiment that has an action that must occur before or during the flow.

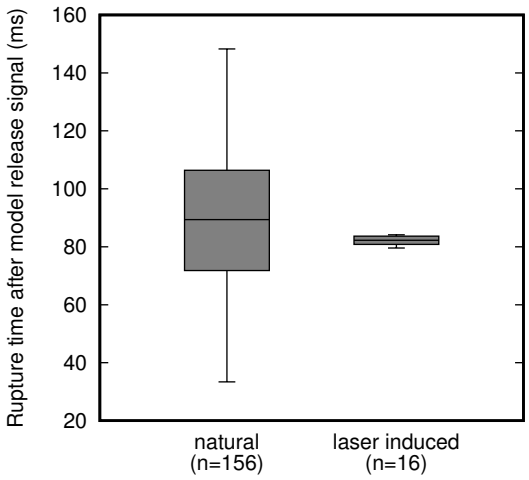

Fig. 8 Facility timing and event sequencing improvements.

For a free-flight experiment in TUSQ, the model is supported by a Chebyshev mechanism which releases the model to fall under gravity. The Chebyshev mechanism requires a finite time to clear the flow region– currently approximately 70 ms. The motion of the test model when falling from rest under the action of gravity only is described by the equation of motion, with the displacement and velocity of the test model presented in Figure 9. For minimum model displacement, the model should be released such that the Chebyshev just clears the flow. Based on a Chebyshev retraction time of 70 ms with a 3 ms margin, the practical improvements to free-flight testing can be demonstrated. To compare the free flight model position and velocity for the natural and laser induced diaphragm rupture methods, the minimum burst time after model release was set to occur at 73 ms after the rising edge of the model release signal. The minimum burst delay of 73 ms after model release assumes the diaphragm ruptures at the instant it it exposed to the laser– practically there is a finite time required for the absorbed energy from the laser to sufficiently weaken the diaphragm.

Late release of the model results in the hypersonic flow arriving before the Chebyshev clears the flow, resulting in a complete loss of useful data from the run. Early release results in greater model displacement (Figure 9a) and

increased model velocity (Figure 9b) and therefore increased momentum. This means that the model has less available core flow to fall through, and a higher downwards momentum to overcome for a model with positive lift, thus limiting the amount of data that can be acquired from a single run. Unlike a late model release, there is no strict definition of an early release as this is a function of the test model size, geometry, mass, angle of attack and aerodynamic coefficients. For the purposes of this analysis, an early release is defined as a release where the model has fallen an additional 20 mm (approximately 25 % of the core flow radius at the nozzle exit) relative to the earliest valid release time. Practically, the early release criteria may often be more strict than indicated by Figure 9.

Unlike the laser on pulse, the natural diaphragm rupture method does not have a clear reference point for timing comparison which makes comparison of event sequencing challenging. To enable comparison of the event sequencing for the natural and laser-induced diaphragm rupture cases, the natural burst method data are aligned in Figure 9 using two independent methods: (1) where the average of the natural diaphragm rupture delays is set to 73 ms, thereby aligned with the earliest possible laser-induced rupture; and (2) where the first quartile from Figure 8 is set to occur at 73 ms. By these two metrics for natural diaphragm rupture timing, when setting the average delay to rupture as 73 ms only 39 % of runs will be successful, reducing to 31 % for method (2). It is likely that there is an intermediate condition exists where success rates in excess of 39% are possible, however it is unlikely that the success rate for the sequencing of free-flight testing would exceed 50% when reliant upon natural diaphragm rupture.

For the 16 runs with laser-induced diaphragm rupture, the timing of the model releases was within ±2.5 ms. This timing repeatability is propagated as a model placement uncertainty at flow onset of ±2 mm for the timing presented in Figure 9.

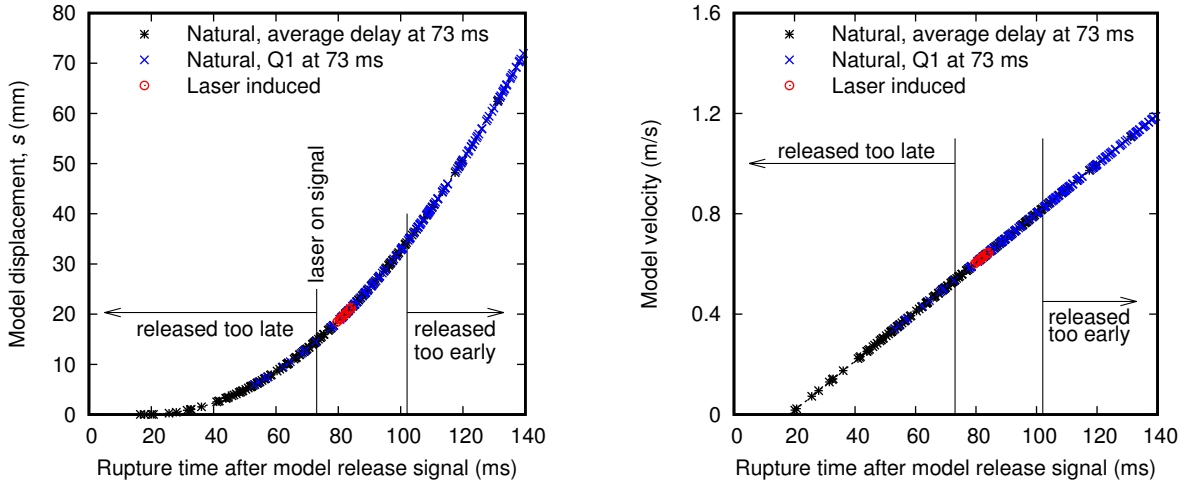

(a) Model displacement. **(b) Model velocity.**

Fig. 9 Motion of a free flight model from release to diaphragm rupture. The model is released from a position slightly above the nozzle centreline so that when the flow first arrives the model is ideally at the nozzle centreline.

The implementation of the laser-induced diaphragm rupture can ensure that no free-flight experiments, or other

timing critical experiments, are rejected due to poor timing. Since implementing the laser-induced diaphragm rupture system, no free-flight test has failed due to improper event sequencing. This marks an approximate doubling of the success of these timing critical experiments relative to relying upon natural diaphragm rupture.

V. Diaphragm Rupture Model Including Thermal Effects

A. Motivation and Approach

The success of the laser-induced diaphragm rupture method has been demonstrated through the experiments described in Section IV. However, there is currently interest in adopting the method at higher pressure and temperature conditions where metallic diaphragms are more appropriate than Mylar diaphragms. To assess prospects for such applications and potentially extend the method to other configurations and operating conditions, a reliable model for the thermally-induced rupture process is needed. In this section, an engineering model for the transient thermally-induced rupture of the Mylar diaphragms due to local laser energy deposition is developed.

The necessary material properties for the Mylar diaphragms are adopted from the manufacturer's data [17] and the representative data presented in Figure 10 illustrates the variation of the ultimate tensile strength with temperature. The melting temperature of Mylar is taken as 529.3 K. Data is also provided for the tensile load carrying capacity at a strain value of $\epsilon = 0.91$ and according to the line-fit shown in Figure 10, the stress (in MPa) varies according to

$$\sigma = 346.6 - 0.6517\,T \tag{1}$$

for T in Kelvin and $T \leq 529.3\,\mathrm{K}$. For $T > 529.3\,\mathrm{K}$, the tensile load intensity is taken as $\sigma = 0$. Stress results are presented for the strain value of $\epsilon = 0.91$ because this is the smaller of the two room temperature elongation-to-failure values presented for Mylar film, which, as manufactured, is an anisotropic film. Using the correlation presented in Equation (1), the ultimate tensile strength of Mylar at room temperature is calculated as $\sigma_u = 156\,\mathrm{MPa}$.

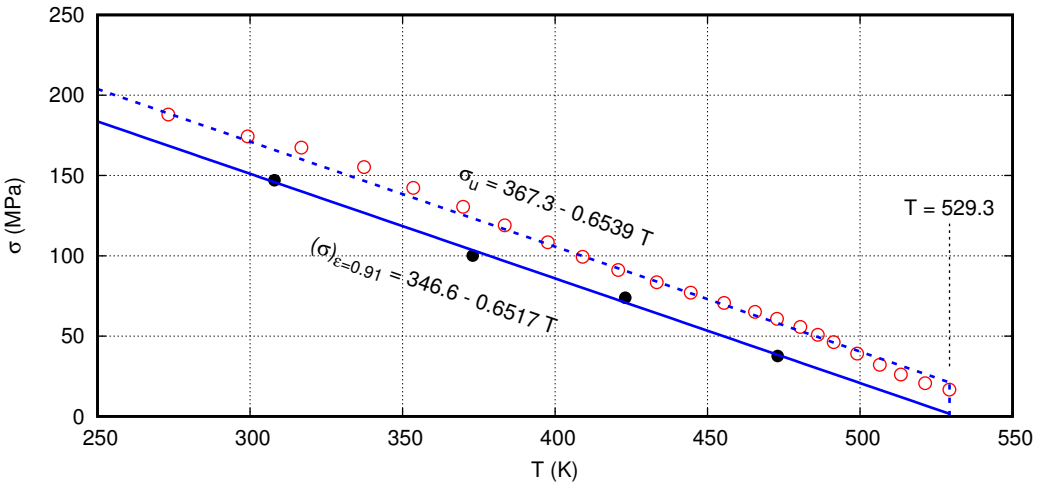

Fig. 10 Variation of Mylar strength with temperature with data (symbols) from [17].

B. Diaphragm Strength

The accuracy of the plastically-deformed spherical-domed diaphragm strength model [18], which is reported to give pressure capacity results within about ±5 % of experimental data from the testing of homogeneous metallic diaphragms, motivates development of the present model. Consider the arrangement illustrated in Figure 11. Development of the new model that accommodates the sensitivity of strength to transient thermal effects proceeds by considering the possibility that the tensile stress within the plastically-deformed diaphragm varies with location x in the material thickness direction. A plastically-deformed element with a thickness of dx of such an inhomogeneous diaphragm can support a pressure differential dP given by

$$\mathrm{d}P = \frac{2\mathrm{d}x\sigma}{R} \tag{2}$$

where R is the mid-plane radius of curvature of the element, and dx is the thickness of the element, provided the tensile stress σ can be carried by the element. In this model, the interfaces between the element at radius x and the surrounding elements located at both larger and smaller values of x are considered frictionless, free of shear stresses. Shear stresses are not expected to have a significant influence on the diaphragm strength because, in practice, diaphragm pressure capacity is observed to increase proportionally with thickness, and essentially the same capacity can be achieved either using a single diaphragm or using a series of two or more diaphragms with a sum of thicknesses equal to that of the single diaphragm.

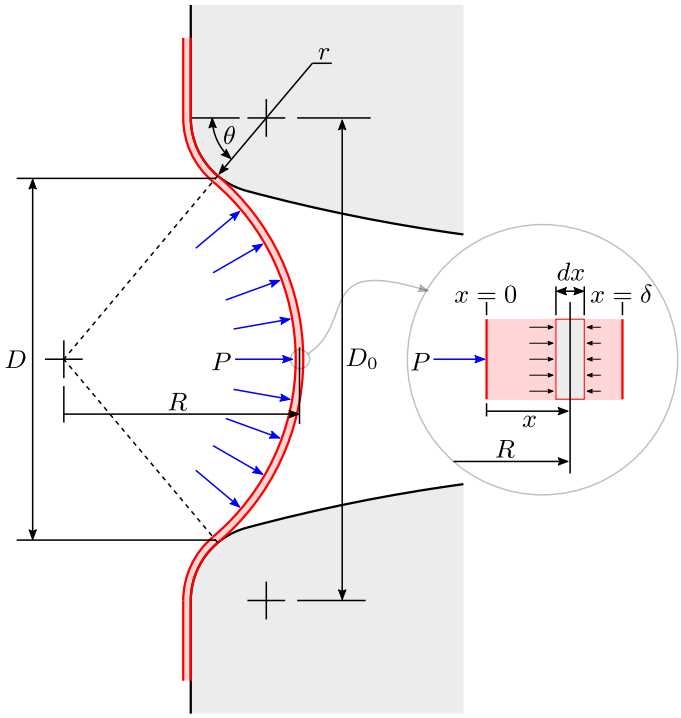

Fig. 11 Illustration of the spherically-domed diaphragm strength model.

Rupture of the plastically-deformed diaphragm is considered to occur when the strain on the diaphragm in the thickness direction (x in Figure 11) reaches the lateral strain value at which rupture occurs in a tensile test. The thickness of a plastically deformed diaphragm δ will be smaller than the original, undeformed thickness of the diaphragm Δ, so the strain in the thickness direction of the diaphragm is $\delta/\Delta - 1$. The diaphragm thickness is generally a small fraction of the radius of curvature, so the radius of curvature of each element will be approximately the same as the radius of curvature of the centre-plane of the diaphragm. For the plastic deformation of the diaphragm, the radius of curvature will be given by [18]

$$R = \frac{D}{4}\sqrt{\frac{1+\epsilon}{\sqrt{1+\epsilon}-1}} \tag{3}$$

where D is the unsupported diaphragm diameter, which is assumed to be the diameter at transition to the constant radius of curvature R segment (see Figure 11) and ϵ is the tension-test direct strain value for the material when it is carrying the stress σ. Equation (3) was obtained by [18] assuming the deformation of the diaphragm preserves the material volume, which appears to be a reasonable approximation during plastic deformation.

Since the radius of curvature of all elements within the diaphragm is approximately the same, Equation (3) indicates that essentially the same tension-test direct strain ϵ will be experienced by all elements throughout the thickness of the diaphragm. Combining Equation (2) and Equation (3), the differential pressure carried by any element can be expressed

as

$$dP = \sqrt{\frac{\sqrt{1+\epsilon}-1}{1+\epsilon}}\frac{8}{D}\sigma\, dx \tag{4}$$

In the case of a homogeneous diaphragm, the tensile stress carried throughout the thickness of the diaphragm will be uniform. However, in the case of a diaphragm composed of elements of material with differing strength, it is possible for the elements to carry different stresses, depending on their respective stress-strain curves, even though each element will be in a state corresponding to the same tension-test strain value. In the case where the mechanical properties vary in a continuous manner due to the presence of temperature variations, the overall pressure carried by the diaphragm is given by

$$P = \sqrt{\frac{\sqrt{1+\epsilon}-1}{1+\epsilon}}\frac{8}{D}\int_0^{\Delta}\sigma(\epsilon, T)\, dx \tag{5}$$

where Δ is the thickness of the diaphragm in the unloaded state. Note that it is appropriate to perform the integration from 0 to Δ rather than from 0 to δ (the deformed thickness of the diaphragm), because stress and strain values for the diaphragm material are presented as *engineering* quantities – the original, unloaded cross sectional area and length are used to define the stress and strain respectively.

C. Natural Rupture

From the geometry of Figure 11, the diameter of the unsupported diaphragm is given by

$$D = 2R\sin\theta \tag{6}$$

Combining Equation (6) with Equation (3) results in

$$\sin\theta = 2\sqrt{\frac{\sqrt{1+\epsilon}-1}{1+\epsilon}}. \tag{7}$$

From the geometry of Figure 11, the unsupported diaphragm diameter is also given by

$$D = D_0 - 2r\sin\theta \tag{8}$$

so we have the unsupported diaphragm diameter specified as

$$D = D_0 - 4r\sqrt{\frac{\sqrt{1+\epsilon}-1}{1+\epsilon}}. \tag{9}$$

Two hypersonic nozzles – Mach 6 and Mach 7 – are currently used in the TUSQ facility, and both adopt the general form illustrated in Figure 11. The lead-in radius for both nozzles is $r = 10\,\text{mm}$, and both have an angle $\theta_{\max} = 75°$, which defines the transition from the lead-in radius to the circular arc that delivers the flow to the nozzle throat. In the case of the Mach 6 nozzle, $D_0 = 63.9\,\text{mm}$ whereas for the Mach 7 nozzle, $D_0 = 48.9\,\text{mm}$. For a tension test elongation to failure of $\epsilon = \epsilon_u = 0.91$, corresponding to the rupture of room temperature Mylar, Eq. (7) gives $\theta = 63.4°$, which is less than the $\theta_{\max}$ for these nozzles confirming the applicability of Eq. (9) and giving the unsupported diaphragm diameter at rupture for the Mach 6 nozzle as $D = 46.0\,\text{mm}$ and for the Mach 7 nozzle as $D = 31.0\,\text{mm}$.

In the case of a homogeneous diaphragm of thickness Δ, the limiting pressure at which rupture occurs will be obtained from Equation (5) when the ultimate strength is reached $\sigma = \sigma_u$ (uniform throughout x) which occurs simultaneously with the elongation-to-failure $\epsilon = \epsilon_u$.

$$P_u = \sqrt{\frac{\sqrt{1+\epsilon_u}-1}{1+\epsilon_u}}\,8\,\frac{\Delta}{D}\,\sigma_u \tag{10}$$

Taking the ultimate strain-to-failure as independent of temperature, the overall sensitivity of the rupture pressure to diaphragm temperature is given by

$$\frac{\mathrm{d}P_u}{\mathrm{d}T} = \sqrt{\frac{\sqrt{1+\epsilon_u}-1}{1+\epsilon_u}}\,8\,\frac{\Delta}{D}\,\frac{\mathrm{d}\sigma_u}{\mathrm{d}T} \tag{11}$$

For $\epsilon_u = 0.91$, $\Delta = 100\,\mu\text{m}$, $D = 46.0\,\text{mm}$ (the Mach 6 nozzle case) and $\frac{\mathrm{d}\sigma_u}{\mathrm{d}T} = -0.652\,\text{MPa}\,°\text{C}^{-1}$ (from Figure 10), we have a Mylar burst pressure sensitivity to temperature of $-5.07\,\text{kPa}\,°\text{C}^{-1}$ which is the slope of the result labelled 'temperature sensitivity' in Figure 4. This value is only about 13 % larger in magnitude than the correlation value from the experiments, as also illustrated in Figure 4, indicating the above model is potentially useful in engineering analysis of other configurations.

As a further assessment of the utility of the above model, it is noted that for a Mylar diaphragm at ambient temperature with a thickness of $\Delta = 100\,\mu\text{m}$, and failure values of $\epsilon_u = 0.91$, $\sigma_u = 156\,\text{MPa}$, Equation (10) gives the value of $P_u\,D = 55.8\,\text{MPa mm}$. For the Mach 6 nozzle case we have $D = 46.0\,\text{mm}$ giving an estimated ambient temperature rupture pressure of 1.21 MPa, and for the Mach 7 nozzle case we have $D = 31.0\,\text{mm}$ giving the value 1.80 MPa. However, the actual rupture pressures observed during facility operation are $\sim 1.0\,\text{MPa}$ in the case of the Mach 6 condition and $\sim 1.3\,\text{MPa}$ in the case of the Mach 7 condition. Therefore, based on the thermally-induced diaphragm rupture model, we deduce that the average temperature rise within the diaphragm during the compression process is 41 °C in the Mach 6 case, and 67 °C in the Mach 7 case. To assess the feasibility of such temperature rises being achieved in practice during the piston compression process, the transient heating model described in [19] is used. The diaphragms are modelled as having lumped thermal capacity, $\rho c \Delta = 163\,\text{J}\,\text{m}^{-2}\,°\text{C}^{-1}$, and the thermal conductivity in the air is assumed to vary linearly with temperature, although its effective magnitude is chosen so that the diaphragm

temperature rise in the model matches the apparent values of 41 °C and 67 °C in each case. Using the measured pressure history for a typical experiment in the Mach 6 case (Figure 6), calculations were performed with the method described in [19] resulting in an effective thermal conductivity value that was 7 times larger than the molecular value. In the Mach 7 case, the resulting value was 10 times larger than the molecular value. Such results appear feasible because turbulent transport effects will boost the effective value of thermal conductivity above the molecular level, and prior work in the case of more rapid compression has adopted effective conductivity values that were 25 times larger than the molecular conductivity [19].

D. Laser-induced Rupture

The starting point for assessing the diaphragm strength model in the context of the localised laser energy deposition method demonstrated herein is Equation (5). To perform the integration specified in Equation (5), a model for the temperature variation through the thickness of the Mylar substrate is required. As the diaphragm typically ruptures within $t = 7\,\text{ms}$ of application of the laser power, the semi-infinite one dimensional model for heat conduction is adequate for the present application. The finite thickness of the diaphragm will not have a significant impact because the thermal penetration distance for the Mylar material (properties takes as $\rho = 1390\,\text{kg}\,\text{m}^{-3}$, $c = 1170\,\text{J}\,\text{kg}^{-1}\,\text{K}^{-1}$, $k = 0.14\,\text{W}\,\text{m}^{-1}\,\text{K}^{-1}$, giving $\alpha = 86 \times 10^{-9}\,\text{m}^2\,\text{s}^{-1}$), which is calculated as $4\sqrt{\alpha t} = 98\,\mu\text{m}$, smaller than the thickness of the Mylar film. Furthermore, the non-uniform distribution of laser power should also have minimal impact on the accuracy of the one-dimensional approach because the power distribution is characterised by a length scale of 290 µm as illustrated in Fig. 5b, which is larger than the thermal penetration distance.

Calculations are performed for the Mylar diaphragm and the Mach 6 nozzle, with the initial diaphragm temperature just prior to application of the laser heating specified as $T_{init} = 62\,^{\circ}\text{C}$. This elevated temperature value is specified so that the model diaphragm rupture pressure without laser heating equals the average measured value of 997 kPa for cases when $T_{amb} \sim 21\,^{\circ}\text{C}$. For a specified step in heat flux due to the laser power absorbed at the surface (q_s), the semi-infinite conduction model provides the temperature within the substrate at any instant (t) after the application of the heating given by

$$T = T_{init} + \frac{2\,q_s}{\sqrt{\pi}\sqrt{\rho c k}}\sqrt{t}\left(\mathrm{e}^{-\hat{x}^2} - \sqrt{\pi}\,\hat{x}\,\mathrm{erfc}(\hat{x})\right) \tag{12}$$

where $\hat{x} = x/(2\sqrt{\alpha t})$ and x is the distance from the surface exposed to the heat flux. To accommodate the effect of the thickness of the acrylic paint in the thermal modelling, the diaphragm thickness was increased by an amount equal to the nominal paint thickness (27 µm), on the assumption that the thermal properties of the acrylic paint are the same as those of the Mylar diaphragm material. At each instant, the integration specified in Equation (5) is then performed with the strength capacity of the Mylar material evaluated using Equation (1), for $\epsilon = 0.91$, on the assumption that the paint makes no contribution to the diaphragm strength. Results from this analysis are presented as the solid lines in

Figure 12 for several magnitudes of the heat flux step that commences at time $t = 0$. Over the first 15 ms of laser heating illustrated in Figure 12, the theoretical maximum pressure differential P that the diaphragm can support decreases with time due to the thermal weakening effect. The data in Figure 12 – the single point with error bars – represents the mean and $\pm 2\sigma$ results from the 16 laser-induced diaphragm rupture experiments.

The measured peak laser flux was of about 1900 kW m^{-2} (Fig. 5), whereas a comparison of the data and the theoretical results (Figure 12) suggests the effective laser heat flux delivered into the surface is around 700 kW m^{-2}, lower than the laser peak laser irradiance by a factor of 2.7. Considering variability in the experimental data (depicted by the error bars in Figure 12) and uncertainties in modelling the layer of paint, this appears to be a reasonable outcome. The model is particularly sensitive to the thickness of the paint and there is substantial variability in these measurements (27 ± 10 µm), but treating the paint layer as having the same effective thermal properties as the Mylar film but with perfect absorptivity of the laser irradiance may also contribute to the observed difference.

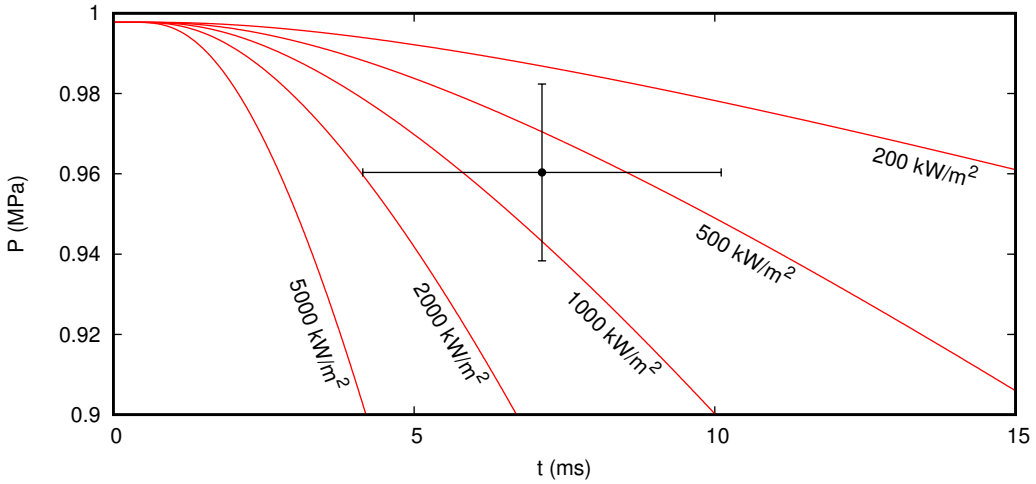

Fig. 12 Decreasing diaphragm capacity with time due to the laser heating, Mach 6 nozzle.

VI. Conclusion

The temperature sensitivity of the Mylar diaphragm strength contributes to the observed variability in rupture pressure when the TUSQ barrel (the Ludwieg tube) is operated in an unheated mode because the test gas temperature (and consequently the diaphragm temperature), varies with the ambient temperature in the laboratory. However, other uncontrolled diaphragm strength parameters still generate an uncertainty in rupture pressure of about ±5 %. Analysis of the variability of the Mylar diaphragm rupture pressure and free flying model release sequencing previously used in the TUSQ facility, demonstrates that successful free flying model experiments could be expected no more than 50 % of the time, at best. The new diaphragm rupture and model release sequencing method introduced herein has demonstrated that the initial positioning of free flying models can now be achieved with an uncertainty of ±2 mm at the onset of the hypersonic flow. Furthermore, the laser-induced diaphragm rupture method described herein is also valuable for in

non-free flying experiments because the repeatability in generating particular flow stagnation pressure conditions is also improved to around ±2 %.

A rupture model that accommodates the thermal sensitivity of the Mylar diaphragm strength is introduced. Using manufacture's data for Mylar properties, the natural rupture pressure from the model is consistent with observed values, provided the heat transfer to the diaphragm during the free piston compression process is considered. When the laser is used, the observed delay between laser switch-on and diaphragm rupture was around 7 ms, and using the model for thermally-induced diaphragm rupture, it is deduced that the apparent peak heat flux delivered by the laser was around 700 kW m^{-2}. This figure is somewhat smaller than the measured peak laser power delivered to the diaphragm. However, it was necessary to paint the diaphragm to enhance the absorption of laser power but the actual thickness of the paint was not be determined precisely; the thermal aspects of the rupture model are sensitive to the thickness of this layer.

Future work at higher pressure and temperature operating conditions will require the use of metallic diaphragms. Preliminary calculations using the presented model for thermal weakening of a 0.1 mm thick low carbon steel diaphragm indicate that about two orders of magnitude more laser power flux will be required to initiate rupture within 10 ms of switch-on. While kilowatt-powered lasers are available for welding and other applications, development of higher fidelity transient thermal modelling is warranted to ensure acquisition of optimal hardware.

Acknowledgments

This research was partially funded by the Australian Government through the Australian Research Council.

References

[1] Kreth, P. A., Gragston, M., Davenport, K., and Schmisseur, J. D., "Design and Initial Characterization of the UTSI Mach 4 Ludwieg Tube," *AIAA Scitech 2021 Forum*, 2021. https://doi.org/10.2514/6.2021-0384.

[2] Hoffman, E. N., LaLonde, E. J., Garcia, M., Elizondo, V. D., Chen, I., Bilbo, H., and Combs, C. S., *Characterization of the UTSA Mach 7 Ludwieg Tube*, 2022. https://doi.org/10.2514/6.2022-1600, URL https://arc.aiaa.org/doi/abs/10.2514/6.2022-1600.

[3] Kimmel, R. L., Borg, M. P., Jewell, J. S., Lam, K.-Y., Bowersox, R. D., Srinivasan, R., Fuchs, S., and Mooney, T., "AFRL Ludwieg Tube Initial Performance," *55th AIAA Aerospace Sciences Meeting*, 2017. https://doi.org/10.2514/6.2017-0102.

[4] Estorf, M., Wolf, T., and Radespiel, R., "Experimental and Numerical Investigations on the Operation of the Hypersonic Ludwieg Tube Braunschweig," *Proceedings of the Fifth European Symposium on Aerothermodynamics for Space Vehicles (ESA SP-563)*, 2005, p. 579.

[5] McGilvray, M., Doherty, L. J., Neely, A. J., Pearce, R., and Ireland, P., "The Oxford High Density Tunnel," *20th AIAA International Space Planes and Hypersonic Systems and Technologies Conference*, 2015. https://doi.org/10.2514/6.2015-3548.

[6] Hyslop, A., Doherty, L. J., McGilvray, M., Neely, A., McQuellin, L. P., Barth, J., and Mullen, G., "Free-Flight Aerodynamic

Testing of the Skylon Space Plane," *Journal of Spacecraft and Rockets*, Vol. 0, No. 0, 2021, pp. 1–11. https://doi.org/10.2514/1.A34937.

[7] Schilden, T., Schroder, W., Ali, S. R. C., Schreyer, A.-M., Wu, J., and Radespiel, R., "Analysis of acoustic and entropy disturbances in a hypersonic wind tunnel," *Physics of Fluids*, Vol. 28, No. 5, 2016, p. 056104. https://doi.org/10.1063/1.4948435.

[8] Schneider, S. P., "Development of Hypersonic Quiet Wind Tunnels," *Journal of Spacecraft and Rockets*, Vol. 45, No. 4, 2008, pp. 641–664. https://doi.org/10.2514/1.34489.

[9] Dannenberg, R., and Stewart, D., *Techniques for Improving the Opening of the Main Diaphragm in a Large Combustion Driver*, NASA TN D-2735, NASA, 1965.

[10] Miller, C. G., "Expansion tunnel performance with and without an electromagneticallyopened tertiary diaphragm," *AIAA Journal*, Vol. 15, No. 7, 1977, pp. 1045–1047. https://doi.org/10.2514/3.7395.

[11] Sasoh, A., Takahashi, T., Watanabe, K., Torikai, H., and Yang, Q.-S., "Shock-Tube Operation with Laser-Beam-Induced Diaphragm Rupture," *AIAA Journal*, Vol. 44, No. 5, 2006, pp. 1110–1112. https://doi.org/10.2514/1.10047.

[12] Mudford, N. R., O'Byrne, S., Neely, A., Buttsworth, D., and Balage, S., "Hypersonic Wind Tunnel Free-Flying Experiments with Onboard Instrumentation," *Journal of Spacecraft and Rockets*, Vol. 52, No. 1, 2015, pp. 231–242. https://doi.org/10.2514/1.A32887.

[13] Zander, F., Leiser, D., Choudhury, R., Loehle, S., and Buttsworth, D., "An Experimental and Numerical Investigation into the Aerodynamics of the ISS Re-entry," *Proceedings of the 21st Australasian Fluid Mechanics Conference*, Australasian Fluid Mechanics Society, 2018.

[14] Leiser, D., Loehle, S., Zander, F., Choudhury, R., Buttsworth, D. R., and Fasoulas, S., "Spacecraft Material Tests under Aerothermal and Mechanical Reentry Loads," *AIAA Scitech 2019 Forum*, American Institute of Aeronautics and Astronautics, 2019. https://doi.org/10.2514/6.2019-0161.

[15] Birch, B., Buttsworth, D., Choudhury, R., and Stern, N., "Characterization of a Ludwieg Tube with Free Piston Compression Heating in Mach 6 Configuration," *22nd AIAA International Space Planes and Hypersonics Systems and Technologies Conference*, American Institute of Aeronautics and Astronautics, 2018. https://doi.org/10.2514/6.2018-5266.

[16] Birch, B., Buttsworth, D., and Zander, F., "Measurements of Freestream Density Fluctuations in a Hypersonic Wind Tunnel," *Experiments in Fluids*, ???? https://doi.org/10.1007/s00348-020-02992-w.

[17] DuPont Teijin Films, "Mylar Physical-Thermal Properties," *Mylar (Product Information)*, 2003.

[18] Vodyanik, V., "Design of safety rupture discs," *Chemical and Petroleum Engineering*, Vol. 8, 1972, pp. 586–588. https://doi.org/10.1007/BF01139117.

[19] Buttsworth, D. R., "Heat transfer During Transient Compression: Measurements and Simulations," *Shock Waves*, Vol. 12, 2002, pp. 87–91. https://doi.org/10.1007/s00193-002-0140-7.